Phosphomolybdic acid-assisted Growth of Ultrathin Bismuth Nanosheets for Electrocatalytic Reduction of CO_2 to Formate with Enhanced Performance

Si-Xuan Guo,[a,b] Ying Zhang,[a,b] Xiaolong Zhang,[a] Christopher D. Easton,[c] Douglas R. MacFarlane[a,b] and Jie Zhang*[a,b]

[a] Dr. S.-X. Guo, Y. Zhang, X. Zhang, Prof. Dr. D. R. MacFarlane, Dr. J. Zhang
School of Chemistry, Monash University, Clayton, Victoria 3800, Australia
E-mail: jie.zhang@monash.edu

[b] Dr. S.-X. Guo, Y. Zhang, Prof. Dr. D. R. MacFarlane, Dr. J. Zhang
ARC Centre of Excellence for Electromaterials Science, Monash University, Clayton, Victoria 3800, Australia

[c] Dr. Christopher D. Easton, CSIRO Manufacturing, Bayview Ave, Clayton, Victoria 3168, Australia

Supporting Information for this article is available on the WWW under http://dx.doi.org/10.1002/cssc.201802409.

Abstract

Oxides containing two dimensional (2D) metallic catalysts have shown enhanced catalytic activity, stability, and product selectivity. Porous 3D structures maximize the accessibility of the active sites, thus enhancing the catalytic performance of the catalysts. By integrating these desirable features in a single catalyst, further improvement in catalytic activity and selectivity is expected. In this study, oxide containing bismuth (Bi) nanosheets of about 4 nm thick interconnected to form a porous three dimensional structure were synthesized by electrodeposition in the presence of phosphomolybdic acid under hydrogen evolution conditions. These Bi nanosheets catalyze CO_2 reduction in a CO_2-saturated 0.5 M $NaHCO_3$ solution to formate with a faradaic efficiency of 93 ± 2% at −0.86 V vs. RHE with a formate partial current density as high as 30 mA cm^{-2}. The Tafel slope of about 78 mV dec^{-1} suggests that the protonation of the adsorbed $CO_2^{\bullet-}$ is the rate limiting step.

Introduction

Carbon dioxide is a notorious gas and its increasing atmospheric concentration is chiefly responsible for climate change. The development of methods to convert CO_2 to useful chemicals/fuels using renewable energy sources has attracted great attention worldwide. Among these methods, electrochemical reduction of CO_2 is promising. However, the application of this method is limited by the high overpotential needed and low product selectivity. In the CO_2 reduction reaction (CO_2RR), weak binding interactions between the reaction intermediates and the catalyst, as well as the slow electron transfer kinetics result in high overpotentials, and low active site density causes low exchange current densities. The low product selectivity is mainly due to the competing hydrogen evolution reaction (HER) and, in the case of copper-based catalysts, the various reaction pathways that are possible for the electrochemical reduction of CO_2.

Two dimensional materials have become promising catalysts for a wide range of applications since they have shown very unique physical and chemical properties, and much improved catalytic activities compared to their bulk counterparts.[1] Their nanoscale size and low dimensional morphology provide more surface active sites and increased number of unsaturated coordinating sites,[2] which can increase the adsorption of the reaction intermediates on the catalyst surface, thus improving catalytic activity and product selectivity. Further improvement in electrocatalytic performance has been achieved by introducing oxides into the structure of two dimensional metallic materials to stabilize either the catalysts or the CO_2 reduction reaction intermediates. Notably, Xie *et. al.* have shown that 4-atom-thick cobalt layers exhibit remarkable intrinsic activity and selectivity for formate production at very low overpotential compared to their bulk counterparts.[3] This intrinsic activity was further increased by partial oxidation of the atomic layers and showed a current density of 10 mA cm^{-2} and a faradaic efficiency (FE) of ~90% for formate over 40 hours at an overpotential as low

as 0.24V. The results suggest that appropriate morphology and oxidation state can convert a nearly non-catalytic material for CO_2 reduction into a very active and robust catalyst. Zheng *et. al.* have also synthesized hybrid Cu/$Ni(OH)_2$ nanosheets which catalyze CO_2 reduction to CO with a faradaic efficiency as high as 92% at an overpotential as low as 0.39V, where $Ni(OH)_2$ plays an important role in stabilizing Cu nanosheets during the electrocatalysis.[4] However, due to the difference in physical and chemical properties of the two elements, this kind of low dimensional material is not common.

Bismuth (Bi) is a non-toxic, inexpensive and quasi-layered material which has shown catalytic activity for electrochemical reduction of CO_2 to formate in aqueous media[5] while having high overpotential for the competing hydrogen evolution reaction. Bi-based materials have also been applied as the catalysts for CO_2 reduction to CO with high faradaic efficiency and current density in organic solvents with ionic liquids as the promoters.[6] Very thin films of Bi have a wide range of physical properties and have attracted significant interests from researchers since the 1960s.[7] The epitaxial Bi thin films have been grown using a molecular-beam epitaxy which requires ultrahigh vacuum conditions.[8] Bi-based nanosheets were also obtained by shear exfoliation of Bi flakes in both top-down and bottom-up approaches using a kitchen blender[9] or by sonication,[10] ultrasound-assisted liquid laser ablation,[11] and hydrothermal reaction.[12] 2D Bi nanosheets have also been generated by electroreduction of pre-synthesized nanosheet templates, such as BiOCl,[5i] BiOBr,[5e] BiOI,[5f] bismuth oxide sulfate and Bi_2S_3,[5h] bismuth subcarbonate (20 – 40 nm thick) synthesized by chemical reaction [5j], and few layer thin bismuth subcarbonate generated by electrochemical exfoliation method[5k]. By contrast, electrodeposition is a convenient technique to generate nanomaterials without the requirement of high vacuum or high temperature. It has been used to synthesize Bi nanoparticles,[13] monolayers,[14] nanowires,[15] nanodendrites[16] and Bi-based thin films.[17] However, synthesis of Bi nanosheets by direct electrodeposition has rarely been reported. To

the best of our knowledge, the only example reported used a pulse-current electrodeposition method to produce Bi nanoflakes,[5b] with a thickness of about 10 – 15 nm.

Polyoxometalates are a class of metal oxide polyanionic clusters which consist of group 6 or 5 transition metals in their high oxidation states. They have rich structural features and electrochemical properties, and have been used as reductants and stabilizing agents for the synthesis of nanomaterials.[18] Recently, we have used phosphomolybdic acid, $H_3PMo_{12}O_{40}$ (PMo), a Keggin type polyoxometalate, to synthesize nanostructured silver with dendrite morphology by electrodeposition.[19] The presence of PMo in the deposition solution enabled the formation of dendrite structure, since the surface energy of the newly formed nano silver is lowered by the adsorption of PMo, thus stabilizing the nanostructure.

Porous 3D structures of metals make the catalytically active sites readily approachable, thus enhancing the catalytic performance of the catalysts.[20] If this feature is combined with metal/metal oxide nanosheets, the performance of the catalysts is expected to be further enhanced.

With these considerations in mind, herein we report a facile polyoxometalate-assisted growth of ultrathin Bi nanosheets (~ 4 nm thick) interconnected to form a porous structure by electrodeposition under hydrogen evolution conditions. These Bi nanosheets catalyze CO_2 reduction in a CO_2-saturated 0.5 M $NaHCO_3$ solution to formate with a faradaic efficiency of 93 ± 2% at −0.86 V vs. RHE with a formate partial current density as high as 30 mA cm^{-2}. The Tafel slope of about 78 mV dec^{-1} suggests that the initial one electron reduction to form the adsorbed $CO_2^{\bullet-}$ is a fast step, followed by a rate limiting chemical reaction step. Under the same conditions, Bi nanodendrites show a much lower faradaic efficiency of 57% for formate with a lower overall current density of 10 mA cm^{-2} under the same conditions. A Tafel slope of 131 mV dec^{-1} was obtained on Bi nanodendrites, indicating a different reaction mechanism applied.

The high catalytic activity and selectivity obtained on Bi nanosheets are mainly attributed to the large amount of edge and corner active sites arising from the two dimensional morphology, the stronger binding sites available from MoO_x for CO_2 and the reduction intermediates, and the porous structure with readily accessible active sites. This study opens up a new avenue for assembling oxide containing two dimensional metallic catalysts into a highly desirable porous 3D electrode for catalysis by a facile electrodeposition method.

Results and Discussion

Electrodeposition and characterization of Bi-PMo nanosheets

Cyclic voltammogram obtained in an aqueous 0.25 M HNO_3 solution containing 1.0 mM $Bi(NO_3)_3$ (Figure 1) on a glassy carbon (GC) electrode shows a simple reduction process with a peak potential of -0.155 V vs. Ag/AgCl (3 M NaCl) assigned to the reduction of Bi^{3+} to Bi^0, and a large stripping process with a peak potential of 0.05 V due to the re-oxidation of Bi^0 back to Bi^{3+}. The cyclic voltammogram of 2.0 mM PMo in 0.25 M HNO_3 solution shows six well-defined PMo reduction processes (**I** – **V**) coupled with proton transfer in the potential range of 0.5 to -0.8 V.[21] The chemically reversible processes **I/I'**, which have much smaller peak currents compared to the others (Figure 1, inset figure), are associated with the adsorbed PMo on the electrode surface.[19] After the addition of 1.0 mM $Bi(NO_3)_3$ to this PMo solution, most of the characteristic reduction processes of PMo (**II** to **VI**) remain unchanged. However, process **I** is replaced by process **1** at a potential of about 0.24 V with much higher current, and the current for process **II** becomes smaller compared to that in the absence of Bi^{3+}. Moreover, a new reduction process **7** is observed at a potential of -0.36 V vs. Ag/AgCl, between processes **V** and **VI**. When the potential is switched after process **V**, no stripping process is observed on the reverse positive potential scan (Figure S1). Therefore, process **7** is assigned to the reduction of Bi^{3+} to Bi^0, which is about 200 mV more negative compared to that of -0.155 V in the

absence of PMo. This suggests that Bi^{3+} has very strong interaction with the negatively charged PMo and its reduced forms, making it more difficult to be reduced. PMo undergoes a square reaction scheme in the presence of Bi^{3+}. The redox processes associated with PMo may shift if the strength of the interaction of PMo with Bi^{3+} is dependent on the redox state of PMo.[22] In the current case, no shift in potential associated with PMo processes was observed, implying that the strengths of the interactions with Bi^{3+} are comparable for the oxidized and reduced forms of PMo. Furthermore, no shift in potentials should be expected when PMo processes emerge at more negative potentials than the $Bi^{3+/0}$ process since the bound PMo is released as a free anion once Bi^{3+} is reduced to Bi metal. The fact that a smaller stripping peak is obtained at a more positive potential (0.12 mC, 0.13 V), compared to those in the absence of PMo (0.36 mC, 0.05 V), suggests that the compositions of the materials deposited during the reduction process may not be the same.

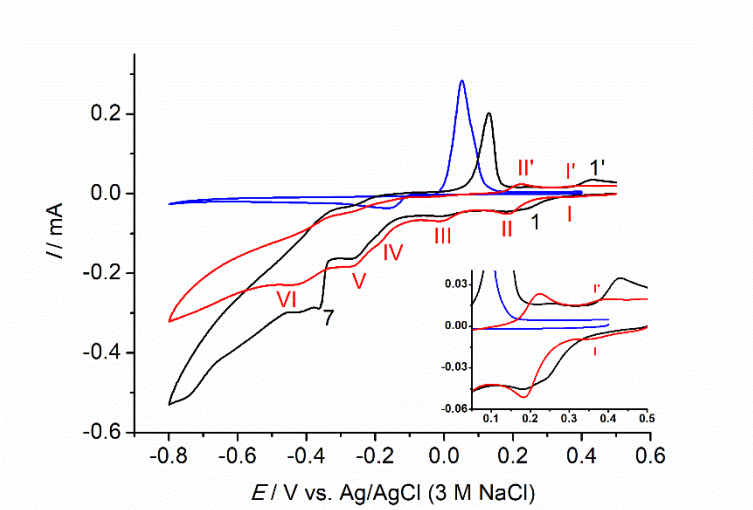

Figure 1. Cyclic voltammograms obtained in aqueous 0.25 M HNO_3 solutions containing: (—) 1.0 mM $Bi(NO_3)_3$ and 2.0 mM PMo, (—) 2.0 mM PMo only, and (—) 1.0 mM $Bi(NO_3)_3$ only. Scan rate: 0.05 V s^{-1}.

Synthesis of Bi nanomaterials was typically carried out by a double potential step deposition method, first at E_1 = -0.8 V for t_1 = 50 s for slow growth of Bi^0 to form an adhesion layer, and then at E_2 = -1.5 V for t_2 = 350 s to form a porous structure. An initial potential (E_1)

of -0.8 V was chosen to generate highly reduced forms of PMo (strong capping agent) for the formation of well-defined Bi nanostructure. A more negative value for E_2 was chosen because a lot of hydrogen bubbles are produced at the electrode surface at this potential, forming a template for the generation of porous Bi nanomaterials with porous 3D structure for the benefit of facile charge transfer and mass transport during electrocatalysis.[20] The SEM image of the film obtained in a 0.25 M HNO_3 solution containing 1.0 mM $Bi(NO_3)_3$ and 2.0 mM PMo shows nanosheets with thickness of roughly about 3 – 10 nm interconnected to form 3D porous structure (Figure 2a). In principle, transmission electron microscopy (TEM) characterization can provide additional morphological information about the nanosheets. However, due to the thinness of Bi-PMo nanosheets and the low melting point of Bi, under the high beam of high resolution TEM, the nanosheets were fused and no high quality TEM images could be obtained. The EDX spectrum (Figure S2) shows the presence of Mo in the deposited film. By contrast, in the absence of PMo, a dendrite like nanostructure was obtained (Figure 2b). This suggests that PMo plays an important role in the formation of nanosheet morphology. For convenience of presentation, the Bi nanosheet material formed in the presence of PMo is called 'Bi-PMo' nanosheets. However, this is not intended to imply that the PMo structure remains intact in the nanosheets. More details are given later.

Our experimental results showed that the Bi nanomaterials deposited by this double potential step method have better adhesion on the electrode substrates, such as GC, graphite rod and FTO than those by a single potential step deposition at either potential. Furthermore, with the single potential step method even when PMo is present, only nanodendrites are formed at a deposition potential of -0.8 V (Figure S3a), while at -1.5 V, some nanosheets are observed along with nanodendrites and the morphology is not uniform (Figure S3b).

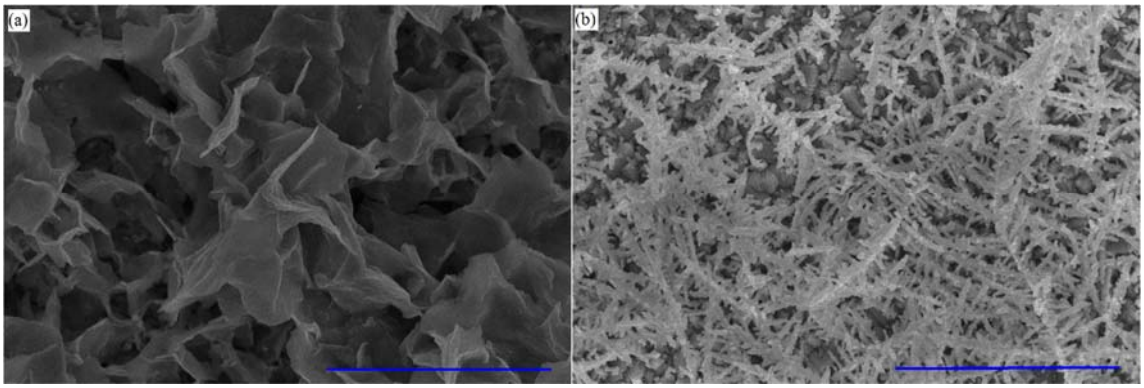

Figure 2. SEM images of the films deposited on FTO electrodes in aqueous 0.25 M HNO_3 solutions containing: a) 1.0 mM $Bi(NO_3)_3$ and 2.0 mM PMo, and b) 1.0 mM $Bi(NO_3)_3$ only. Deposition was carried out using a two potential step method described in the Experimental Section. The scale bars represent 2 μm.

The crystalline structures of Bi nanomaterials were characterized using XRD (Figure S4). The XRD patterns of Bi-PMo nanosheets can be indexed to the (003), (012), (104), (110), (024), (116) and (112) planes of rhombohedral Bi (JCPDS card No. 44-1246) (Figure S4a). No obvious patterns for PMo or Mo oxides are observed, most likely due to the very low amount of these materials on the nanosheets or the low crystallinity because of the nanosize. Bi nanodendrites show similar patterns, which suggests that the presence of PMo during the electrodeposition of Bi materials does not significantly affect their crystalline structures.

The topographic AFM image shows the nanosheet with a thickness of about 4 nm (Figure 3a). The height profile of the AFM image shows that the apparent height of the nanosheet above the substrate is around 4 nm, and is consistent with that observed in the SEM image. These results suggest that the nanosheet contains only 9 atomic layers based on the interlayer distance of 4.64 Å.[23]

Raman scattering spectra were obtained on Bi-PMo nanosheets and $H_3PMo_{12}O_{40}$ (PMo) (Figure 3b) to characterize the compositions of Bi-PMo nanosheets. The strong bands at 997, 976, 903, 851, 776, 605 and 251 cm^{-1} observed for highly crystalline PMo are consistent with those reported in the literature.[24] It is clear from Figure 3b that those bands typical for PMo

are absent in the Raman spectrum obtained on Bi-PMo nanosheets, except the broad band at 605 cm^{-1}, which is assigned to a combined stretching and bending of the Mo–O_{2c1} bonds.[24a] This result indicates that the Mo detected on Bi-PMo nanosheets in EDX spectrum may not be in the original form of PMo. Three new sharp bands at 874, 304, 131 cm^{-1}, and three shoulders at 793, 390 and 106 cm^{-1}, which are not seen with PMo, are now observed on the nanosheets. The bands at 874, 793 and 605 cm^{-1}, which closely resemble, though do not totally match due to the complexity of the composition of Bi-PMo nanosheets, those of MoO_x,[25] are tentatively assigned to the vibration modes of MoO_x, while the bands at 390, 304 and 131 cm^{-1} are assigned to the Bi-O stretches of the heavy metal oxide Bi_2O_3, and the one at 106 cm^{-1} is attributed to the vibration mode of heavy metal Bi or the lattice vibration.[26] Bi_2O_3, which is not detected by XRD, could be due to the oxidation of surface Bi metal on Bi-PMo nanosheets in air during sample preparation and analysis. The Raman bands of Bi-PMo nanosheets are different from those of Bi_2MoO_6,[27] suggesting that they may consist of Bi_2O_3 and Mo oxides, but not Bi_2MoO_6.

X-ray photoelectron spectroscopy (XPS) was used to characterize the surface of Bi-PMo nanosheets (Figures 3 c & d). For comparison, the XPS spectrum of $H_3PMo_{12}O_{40}$ (PMo) was also obtained (Figure S5a). The analysis of the XPS spectra of molybdenum oxide was carried out using the insights reported by Baltrusaitis et. al.[28] For $H_3PMo_{12}O_{40}$, both Mo and P were detected at a ratio of P/Mo = 0.106. The high resolution Mo 3d peak could be fitted with a single doublet, with a binding energy (BE) of 233.4 eV for the $3d_{5/2}$ peak. This BE position is significantly higher than that of Mo(VI) in MoO_3, however is consistent with Mo in compounds similar to PMo based on entries within the NIST database.[29] Thus, these results indicate that the PMo data can be used as a reference for the interpretation of the XPS spectra of Bi-PMo nanosheets before and after controlled potential electrolysis. For Bi-PMo nanosheets, the elemental quantification (Table S1) confirms the presence of the elements Bi, P and Mo. The

P/Mo value is 0.121, compared to 0.106 measured for PMo (Table S1), suggesting that not all of the Mo may be in the original form of PMo. This point is confirmed by the high resolution Mo 3d spectrum (Figure 3c), where the spectrum is fitted with 4 separate doublets. The Mo in PMo is still present in the fit, however, only represents a small fraction of the overall signal. The three new contributions are assigned to Mo(VI), Mo(V) and Mo(IV) based on the binding energy (BE) positions identified in Table S2. The contributions from Mo(VI) and Mo(V) are approximately equal and represent the most dominant contributions to the fit. As detailed by Baltrusaitis et. al.,[28] the precise contributions to the Mo(V) assignment are not clear, however likely represent a broad range of Mo phases. The high resolution Bi 4f spectrum (Figure 3d) shows two distinct doublets attributed to the Bi $4f_{7/2}$ peaks as detailed in Table S2. The lower BE contribution is assigned to Bi(0),[30] while a significantly more intense contribution at higher BE is assigned to Bi(III). Unfortunately, based on the peak position it is not clear whether Bi(III) is in the form of bismuth oxide or bismuth molybdates (Bi_2MoO_6) since there is significant overlap in the range of reported Bi $4f_{7/2}$ BE values for bismuth oxide[31] and bismuth molybdates.[31c, 32] However, as suggested by the Raman results, the presence of Bi_2MoO_6 may be ruled out. Therefore, Bi(III) may be in the form of bismuth oxide.

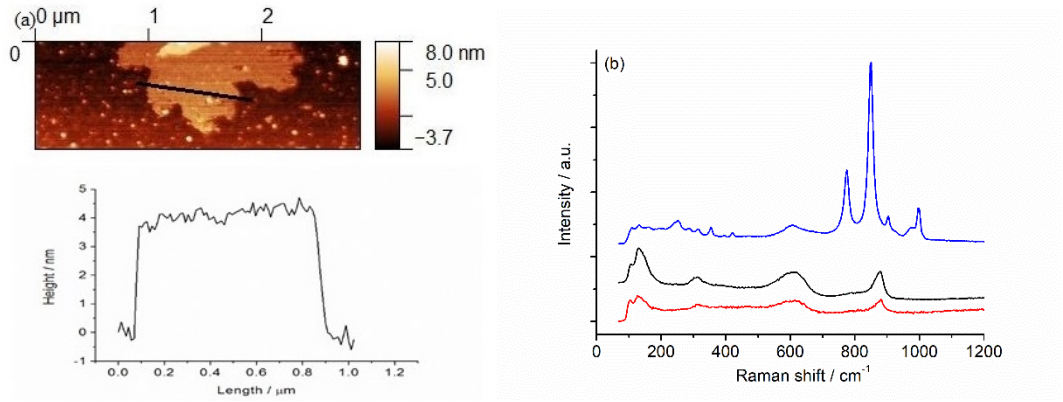

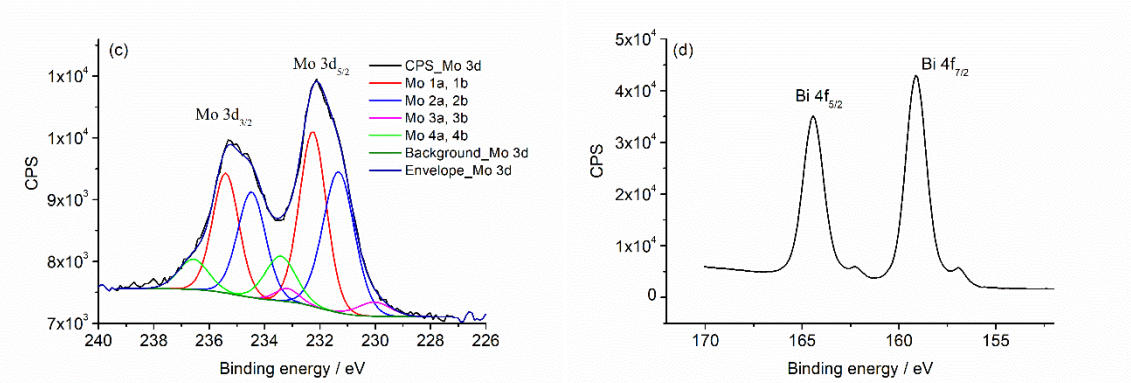

Figure 3. a) AFM image and height profile; b) Raman spectra of Bi-PMo nanosheets before (—) and after electrolysis (—), and $H_3PMo_{12}O_{40}$ (—); high resolution XPS spectra recorded for c) Mo 3d and d) Bi 4f regions of Bi-PMo nanosheets.

Since the presence of PMo has a significant role in the formation of Bi-PMo nanosheet structure, different PMo concentrations were studied. When the concentration of PMo is as low as 0.02 mM, under the same deposition conditions, only a very small amount of nanosheets is formed (Figure S6a) with the majority of nanodendrites. As the concentration of PMo increases to 0.2 mM, more nanosheets are obtained (Figure S6b). At a PMo concentration of 2.0 mM, Bi-PMo nanosheets are observed with no presence of nanodendrites (Figure 2a). Therefore, a PMo concentration of 2.0 mM was used for the following studies unless otherwise stated.

The deposition of Bi-PMo nanocomposites was attempted in the absence of HNO_3 (in an aqueous solution containing only 1.0 mM $Bi(NO_3)_3$ and 5.0 mM PMo), similar to the electrodeposition of Ag-PMo nanodendrites.[19] A PMo concentration of 5.0 mM (pH ≈ 1.75) was used instead of 2.0 mM to make sure that $[PMo_{12}O_{40}]^{3-}$ and its protonated forms are the dominant species,[33] similar to that in the presence of HNO_3. The SEM image (Figure S7a) shows that nanoparticles of the size of about 100 nm as well as larger blocks were formed. This suggests that the presence of a high concentration of acid is also required for the formation of Bi nanomaterials. However, at a higher acid concentration of 0.5 M, irregular shapes of the Bi nanomaterials are observed (Figure S7b). This is due to the much higher rate of hydrogen evolution on the electrode surface at this high acid concentration under the same deposition

conditions, which caused the deposited film to detach from the substrate surface thus affecting the deposition of Bi nanostructure.

Electrochemical CO_2 reduction in 0.5 M $NaHCO_3$ media

In order to evaluate the catalytic activities of Bi-PMo nanosheets and Bi nanodendrites for CO_2 reduction, cyclic voltammetric experiments were carried out in N_2 or CO_2 saturated 0.5 M $NaHCO_3$ aqueous solutions (Figure 4). For both Bi nanomaterials, much larger current responses were observed under CO_2 compared to those under a N_2 atmosphere, which is ascribed to their catalytic activities for CO_2 reduction. Under a CO_2 atmosphere, the reduction current of about 32.5 mA cm^{-2} at −0.86 V vs. RHE was obtained on Bi-PMo nanosheets, which is much higher than that of about 10 mA cm^{-2} obtained on Bi nanodendrites. The overpotential required for the CO_2 reduction reaction to achieve a current density of 5 mA cm^{-2} is about 0.2 V less on Bi-PMo nanosheets than that on Bi nanodendrites. This much enhanced CO_2 reduction activity of Bi-PMo nanosheets could be at least partially attributed to the larger electroactive surface area (ESA), since the capacitive current in the potential range between 0 and -0.5 V, which is indicative of the ESA, is much larger (~ 4 times larger) on Bi-PMo nanosheets (more quantitative analysis of double layer capacitance is given in Figure S8).

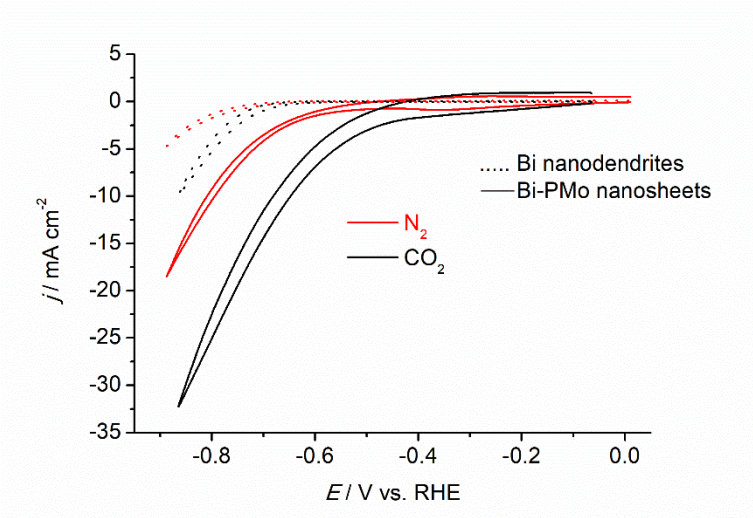

Figure 4. Cyclic voltammograms obtained on Bi nanosheets (solid lines) and nanodendrites (dash lines) modified GC electrode in CO_2 (black lines) or N_2 (red lines) saturated 0.5 M $NaHCO_3$ aqueous solutions. Scan rate: 0.1 V s^{-1}.

Voltammetric studies were also carried out to investigate the effects of deposition conditions on the catalytic activities of the Bi nanomaterials. When the concentration of PMo increases from 0.02 mM to 0.1 mM (Figure S9a), the catalytic CO_2 reduction current density at **-**0.86 V vs. RHE does not change much, but the capacitive current in the potential range of **-**0.06 to -0.56 V increases with the increase of PMo concentration. This capacitive current (at **-**0.1 V) further increases with increasing PMo concentration up to 2.0 mM (Figures 4 & S9b), indicating the formation of more nanosheets which enhances the ESA and the presence of more adsorbed PMo. This is consistent with the SEM images taken from the samples prepared using different concentrations of PMo. As the concentration of PMo increases from 0.1 mM to 2.0 mM, the catalytic current increases significantly (about 2.5 times at -0.86 V), along with the positive shift of onset potentials from about -0.63 V to -0.45 V. Further increase of PMo concentration from 2.0 to 5.0 mM does not lead to further increase in ESA and catalytic current.

The second deposition potential (E_2) was varied from -1.0 V to -2.0 V to find the optimum condition for the deposition of Bi-PMo nanomaterials which achieves the highest catalytic activity towards CO_2 reduction. The highest catalytic CO_2 reduction current was obtained on Bi-PMo nanosheets formed using E_2 values of -1.5 or -1.6 V vs. Ag/AgCl. When the second deposition time (t_2) increases from 0 to 300 s, the catalytic CO_2 reduction current also increases, due to the deposition of more Bi-PMo nanosheets on the electrode surface, as also indicated by the increased capacitive current in the potential range of -0.06 to -0.56 V. The onset potential also shifts from around -0.63 to -0.45 V vs. RHE. Further increasing t_2 to 400 s does not have much influence on either the catalytic current or onset potential.

Controlled potential electrolysis was carried out in CO_2 saturated 0.5 M $NaHCO_3$ solutions at various potentials to evaluate the catalytic activities and selectivity of Bi-PMo nanosheets and other Bi nanomaterials for CO_2 reduction. For Bi-PMo nanosheets deposited in 0.25 M HNO_3 solution containing 1 mM $Bi(NO_3)_3$ and 2.0 mM PMo, formate and hydrogen were detected as the main products (Figure 5) with overall FE close to 100%. A very small amount of CO (< 2%) was also detected. At a potential as low as -0.53V, a $FE_{formate}$ of about 20 ± 4% was obtained, with about 51 ± 2% FE_{H2} (Figure S10). As the applied potential becomes more negative, the $FE_{formate}$ increases significantly, and reaches about 93 ± 2% at a potential of -0.86 V vs. RHE. At more negative potentials, the $FE_{formate}$ decreases due to the increase in hydrogen evolution on Bi-PMo nanosheets (i.e. increase in FE_{H2}). While for Bi nanodendrites, a $FE_{formate}$ of 48 ± 2% was obtained at a potential of -0.77 V vs. RHE, which is 0.1 V more negative than that obtained on Bi-PMo nanosheets. A maximum $FE_{formate}$ of 81 ± 2% was obtained at a potential of -0.96 V. Representative gas chromatographs of H_2 and CO obtained from the headspace gas, and a ^1H NMR spectrum obtained from the catholyte with added DMSO as an internal standard, of CO_2 reduction using Bi-PMo nanosheets as the catalysts are presented in Figure S11.

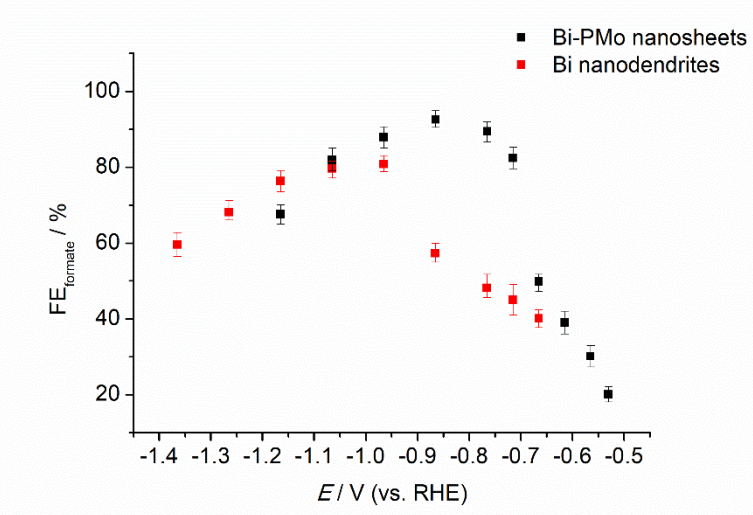

Figure 5. Faradaic efficiencies for formate obtained on Bi-PMo nanosheets (▪) and Bi nanodendrites (▪) at various applied potentials in CO_2 saturated 0.5 M $NaHCO_3$ solutions.

The long term stability of the catalysts under catalytic turnover conditions is very important for their practical applications. The stability of Bi-PMo nanosheets was studied by controlled potential electrolysis at **-**0.86 V for 10 hours. A total current density of around 32 mA cm^{-2} was maintained throughout the 10 hours testing period without obvious decay (Figure 6). The $FE_{formate}$ values determined during the first half and final half hour of the electrolysis were about 95%. The SEM image (Figure S12a) and Raman spectrum (Figure 3b) obtained after electrolysis on Bi-PMo nanosheets show similar characteristics as those obtained before electrolysis (Figures 2a & 3b). The capacitive current in the potential range between 0 and -0.5 V measured on Bi-PMo nanosheets after the electrolysis (Figure S12b) is similar to that obtained before electrolysis (Figure S8a), indicating that the ESA remains unchanged. These results suggest that the morphology, reactivity and probably the composition of Bi-PMo nanosheets remain unchanged under catalytic turnover conditions. The stability of Bi-PMo nanosheets at other applied potentials was also studied by controlled potential electrolysis for about 1 hour, and the results (Figure S13a) showed that the nanosheets are stable under all potentials studied. The partial current density for formate ($j_{formate}$) as a function of applied potential is shown in Figure S13b, which shows that when the applied potential is at or more negative than -0.86 V vs. RHE, $j_{formate}$ approaches the mass transport limiting value under our experimental conditions, which is consistent with previous finding.[20]

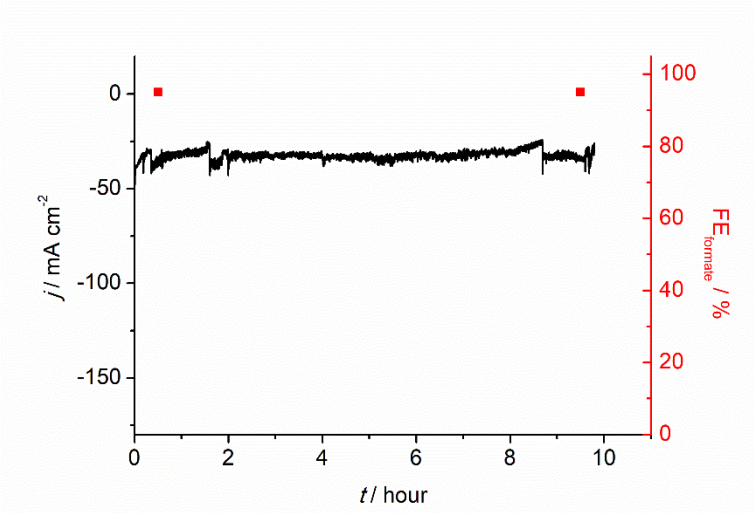

Figure 6. Long term stability study of Bi-PMo nanosheets during controlled potential electrolysis at -0.86 V vs. RHE in a CO_2 saturated 0.5 M $NaHCO_3$ solution.

Mechanistic studies

The higher $FE_{formate}$ at lower overpotentials obtained on Bi-PMo nanosheets than those on Bi nanodendrites cannot be solely attributed to their larger ESA. To obtain the mechanistic insight into the enhanced CO_2 reduction performance associated Bi-PMo nanosheets, their surface composition after long term electrolysis was analysed using XPS, which showed significant changes in the elemental quantification compared to those found before electrolysis (Table S1). No signal for P was detected after electrolysis. The high resolution Mo 3d spectrum (Figure S5b) is now fitted with 3 separate doublets, assigned to Mo(VI), Mo(V) and Mo(IV). The doublet associated with PMo is not applicable as intensity is no longer observed at the Mo $3d_{2/3}$ peak position assigned to PMo (Figure S5a). Compared with Bi-PMo nanosheets before electrolysis (Figure 3c), it appears that partial reduction of Mo(V) and Mo(VI) to Mo(IV) occurred during electrolysis as the concentration of states now follows Mo(VI) > Mo(IV) > Mo(V). The Mo 3d spectrum reported here is remarkably similar to that reported by Baltrusaitis et. al.[28] for amorphous molybdenum oxide synthesized by electrodeposition (see Figure 9 in Reference [28]). No significant difference was observed in the Bi 4f spectrum based on the peak positions listed in Table S1 and Figures 3d and S5c.

Since MoO_x originated from PMo is also present in Bi-PMo nanosheets under catalytic turnover conditions, experiments were carried out to study the catalytic activity of MoO_x modified glassy carbon electrode on CO_2 reduction. To fabricate a MoO_x modified GC, a PMo modified GC was formed according to the procedure described in the Experimental Section. Cyclic voltammogram obtained on the PMo-modified GC in a 2 M H_2SO_4 aqueous solution shows three well defined surface-confined processes in the potential range of 0.55 - -0.1 V vs. Ag/AgCl (3M NaCl) (Figure S14a), confirming the presence of PMo on the GC surface. A surface coverage of 4.2×10^{-11} mol cm^{-2} was calculated by integration of the charge of the second reduction process. Cyclic voltammogram obtained on the PMo modified GC in a CO_2 saturated 0.5 M $NaHCO_3$ solution shows a current density about twice that of a bare GC under the same conditions (Figure S14b), but is negligibly small compared to that obtained on Bi-PMo nanosheets (Figure 4). The voltammogram obtained in 2 M H_2SO_4 on the PMo modified GC after the CO_2 reduction experiment shows that all three surface confined redox processes are now gone. This is expected as PMo is not stable in aqueous solutions with pH > 3, and decomposes to various molybdenum oxide species.[33] In order to identify whether PMo and its decomposed oxide species can catalyze CO_2 reduction, controlled potential electrolysis was also carried out in a CO_2-saturated 0.5 M $NaHCO_3$ solution using PMo modified GC plate (~ 9 cm^2) at -0.86 V vs. RHE, where maximum $FE_{formate}$ was obtained on Bi-PMo nanosheets. The analysis of electrolysis products show that hydrogen is the major product, and only about 0.9% $FE_{formate}$ was obtained. This result suggests that Bi rather than MoO_x is the catalyst for the formation of formate.

Tafel plots were constructed using the $FE_{formate}$ data obtained at various potentials (Figure 7). The formal potential of -0.09 V vs. RHE for the $CO_2/HCOO^-$ couple[34] in a CO_2 saturated 0.5 M $NaHCO_3$ solution (pH 7.2) was used for the estimation of overpotential values used in the construction of Tafel plots. A Tafel slope of 131 mV dec^{-1} for formate was obtained for Bi

nanodendrites, which suggest that the formation of $CO_2^{\bullet-}$ is the rate determining step.[35] By contrast, a significantly smaller Tafel slope of 78 mV dec^{-1} for formate was obtained for Bi-PMo nanosheets in the potential range where the process is kinetically controlled, which is close to the theoretical value of 59 mV dec^{-1} when the protonation of $CO_2^{\bullet-}$ is the rate determining step.[35] Li and coworkers have reported that Bi(001) plane and low-index crystal planes are very active for CO_2 reduction which was supported by the DFT calculation.[5f] Sargent and coworkers also reported that Bi(110) plane is very active for CO_2 reduction.[5e] However, the DFT calculation carried out by Min and coworkers showed that high index planes of Bi such as (012), (110) and (104), are responsible for the high CO_2 reduction activity to form formate by efficiently stabilizing the *OCOH intermediate.[5d] Moreover, Lee and coworkers showed that large number of edge or corner sites of Bi nanoflakes facilitate strong local electric fields, leading to close to 100% faradaic efficiency for formate, which was confirmed by numerical simulation.[5b] Bao and coauthors have also demonstrated that it is much easier for CO_2 to adsorb and the key reaction intermediate COOH* to form on edge and corner sites than on terrace sites of Pd NPs.[36] Therefore, based on the literature, it is reasonable to deduce that the high activity of Bi-PMo nanosheets are due to the high number of edge and corners sites arising from their 2D structure. The presence of MoO_x could also provide stronger binding sites for CO_2 and the reaction intermediate in a similar way as PMo.[19] Though the presence of MoO_x may enhance the initial one electron reduction of CO_2 on Bi-PMo nanosheets to become a fast step, it may also contribute to the hydrogen evolution in the potential region studied. Compared to other studies using Bi-based catalysts,[5] the formate selectivity obtained in this work is among the highest reported, with an average value of 93 ± 2%.

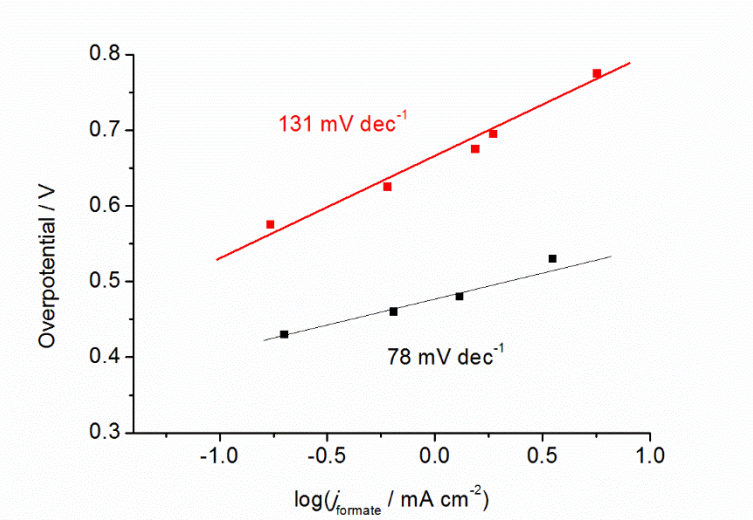

Figure 7. Tafel plots obtained on Bi-PMo nanosheets (▪) and Bi nanodendrites (▪).

Conclusion

In this study, polyoxometalate was used to assist electrodeposition of porous ultrathin Bi-PMo nanosheets (~ 4 nm thick) under hydrogen evolution conditions. These Bi-PMo nanosheets catalyze CO_2 reduction in a CO_2-saturated 0.5 M $NaHCO_3$ solution to formate with a faradaic efficiency of 93 ± 2% at −0.86 V vs. RHE with a formate partial current density as high as 30 mA cm^{-2}. The Tafel slope of about 78 mV dec^{-1} suggests that the initial one electron reduction to form the adsorbed $CO_2^{\bullet-}$ is a fast step, followed by a rate limiting chemical reaction step. Under the same conditions, Bi nanodendrites showed a much lower faradaic efficiency of 57% for formate with a lower formate partial current density of 5.7 mA cm^{-2}. A Tafel slope of 131 mV dec^{-1} was obtained on Bi nanodendrites, indicating a different reaction mechanism applied. The much higher catalytic activity and selectivity at lower overpotentials obtained on Bi-PMo nanosheets over Bi nanodendrites are attributed to the large surface area of Bi-PMo nanosheets, the high amount of catalytically more active edge and corner sites arising from the two dimensional morphology, the presence of MoO_x oxides for binding of CO_2 and its reduction intermediates, and the porous 3D structure with readily accessible active sites.

Experimental Section

Chemicals. Bismuth nitrate ($Bi(NO_3)_3$), phosphomolybdic acid ($H_3[PMo_{12}O_{40}]$, PMo, 99.9%,), nitric acid (HNO_3, 70%), sodium bicarbonate ($NaHCO_3$) and sulfuric acid (H_2SO_4, 95 – 98%) from Sigma-Aldrich, and CO_2 (Food grade, Aligal, Air Liquide) were used as supplied. Deionized water from a MilliQ-MilliRho purification system (resistivity 18 MΩ·cm) was used to prepare all aqueous solutions.

Electrochemistry. All electrochemical experiments were carried out at 22 ± 2 °C using a CHI 760E electrochemical workstation (CH Instruments, Austin, TX). A standard three-electrode electrochemical cell with a glassy carbon (GC) or fluorine doped tin oxide (FTO) working electrode, a Pt wire counter electrode and an Ag/AgCl (3 M NaCl) reference electrode was used. Prior to voltammetric experiments or electrodeposition, the working electrode was polished with 0.3 μm alumina slurry on a polishing cloth (Buehler, USA), rinsed with water, sonicated in water thoroughly to remove alumina, rinsed with water again, and finally dried under nitrogen gas. No pretreatment of the electrode substrate was required.

Electrochemical CO_2 reduction. For electrochemical studies (except bulk electrolysis), the solution was purged with nitrogen or carbon dioxide for at least 15 min before measurements, and then the electrochemical cell was kept under a positive pressure of nitrogen or carbon dioxide at all times.

Controlled potential bulk electrolysis was carried out in an airtight H-cell with two compartments separated by a frit. The aqueous 0.5 M $NaHCO_3$ solution was purged with CO_2 for 30 min and then sealed properly. A piece of 2 cm × 1 cm glassy carbon plate modified with Bi-PMo nanosheets or Bi nanodendrites was used as the working electrode and a large Pt mesh as the counter electrode, along with the same reference electrode as used in voltammetric

studies. For the convenience of comparison of our results with other studies, the reversible hydrogen electrode (RHE) reference scale is used for all the electrochemical CO_2 reduction studies, and Eq. 1 was used for the conversion of the potential.

$$E\ (vs.\ \text{RHE}) = E\ (vs.\ \text{Ag/AgCl}) + 0.220\ \text{V} + 0.0585\ \text{V} \times pH \qquad \text{(Eq. 1)}$$

The gas products generated by bulk electrolysis, i.e. carbon monoxide and hydrogen, were analyzed by gas chromatographic technique on an Agilent 7820 gas chromatograph with a HP-PLOT Molesieve/5Å column equipped with a thermal conductivity detector (TCD). Helium gas of 99.99% purity was used as the carrier gas for CO detection, while nitrogen gas (99.99%) was used as the carrier gas for H_2 detection. The liquid products were analyzed by ^{1}H NMR on a Bruker DRX400 at a frequency of 400.2 MHz with added DMSO as the internal standard.

Fabrication of modified electrodes. The electrodeposition of Bi nanosheets was carried out in an aqueous 0.25 M HNO_3 solution typically containing 1.0 mM $Bi(NO_3)_3$ and 2.0 mM PMo where PMo is stable,[33a] by a two-step reduction to reduce Bi^{3+} to Bi^0 and PMo to PMo^{n-} simultaneously. The solution was magnetically stirred at a rotation rate of 200 rpm during the course of electrodeposition. Care should be taken to ensure that no oxygen is present in the cell for successful deposition of nanosheets. In a typical two-step reduction, an initial potential of -0.8 V vs. Ag/AgCl (3 M NaCl) was applied for 50 s to initiate the nucleation for the growth of Bi nanosheets on the substrate, and the applied potential was then switched to -1.5 V for 350 s, to obtain films with optimal catalytic activity and stability. The modified electrodes were immediately rinsed thoroughly with water and dried in air before use. Substrates such as GCs, FTO glasses and graphite rods have been used in this study, and no morphology or structure difference was observed on different substrates.

Bi nanodendrites were synthesized in a similar manner in the absence of PMo. PMo modified glassy carbon electrodes/plates were fabricated by soaking the electrodes/plates in a 2 M H_2SO_4 solution containing 5 mM PMo to form a layer of adsorbed PMo, utilizing the strong adsorption property of PMo on GC.[37]

The electroactive surface area (ESA) of a Bi nanomaterial modified electrode was determined by measuring the double layer capacitance obtained at different scan rates (0.01 – 0.1 V s^{-1}) in a N_2 saturated 0.5 M $NaHCO_3$ solution.

Characterization of Bi nanomaterials. Scanning electron microscopy (SEM) images and energy-dispersive X-ray spectra (EDX) of the electrodeposited Bi-PMo nanosheets and Bi nanodendrites modified FTO glass slides were obtained using a FEI Nova NanoSEM 450 FEG SEM equipped with Bruker Quantax 400 X–ray analysis system. X-Ray Diffraction (XRD) measurements were undertaken with a Bruker D8 ADVANCE X-ray powder diffractometer (Cu Kα1 radiation) using a scan step of 0.02 degree per step and a residual time of 1 second per step. The thickness of Bi-PMo nanosheets was characterized by atomic force microscopy (AFM) in air with a Bruker Dimension Icon SPM equipped with a Pt/Ir coated silicon cantilever as the conductive probe. Raman spectra were obtained using a Renishaw inVia Microscope with a 532 nm laser source.

X-ray photoelectron spectroscopy (XPS) analysis was performed using an AXIS Nova spectrometer (Kratos Analytical Inc., Manchester, UK) with a monochromated Al K_α source at a power of 180 W (15 kV × 12 mA) and a hemispherical analyser operating in the fixed analyser transmission mode. The total pressure in the main vacuum chamber during analysis was typically between 10^{-9} and 10^{-8} mbar. Survey spectra were acquired at a pass energy of 160 eV. To obtain more detailed information about chemical structure, oxidation states etc., high resolution spectra were recorded from individual peaks at 20 eV (yielding a typical peak width

for polymers of 1.0 eV). Each specimen was analysed at an emission angle of 0° as measured from the surface normal. Assuming typical values for the electron attenuation length of relevant photoelectrons the XPS analysis depth (from which 95% of the detected signal originates) ranges between 5 and 10 nm for a flat surface. Since the actual emission angle is ill-defined in the case of rough surfaces (ranging from 0º to 90º) the sampling depth may range from 0 nm to approx. 10 nm. Data processing was performed using CasaXPS processing software version 2.3.15 (Casa Software Ltd., Teignmouth, UK). All elements present were identified from survey spectra. The atomic concentrations of the detected elements were calculated using integral peak intensities and the sensitivity factors supplied by the manufacturer. Binding energies were referenced to the C 1s peak at 284.8 eV (aliphatic hydrocarbon) and 284.4 eV (graphitic carbon). The accuracy associated with quantitative XPS is ca. 10% - 15%. Precision (ie. reproducibility) depends on the signal/noise ratio but is usually much better than 5%. The latter is relevant when comparing similar samples.

Acknowledgements

This research was supported by the Australian Research Council (ARC) through the ARC Centre of Excellence for Electromaterials Science (grant no. CE140100012), and D.R.M's Australian Laureate Fellowship (award no. FL120100019). The authors acknowledge the use of facilities within the Monash X-Ray Platform and the Monash Centre for Electron Microscopy.

Supporting information

Additional characterization data for Bi-PMo nanosheets and Bi nanomaterials deposited under different conditions, as well as PMo by XPS, SEM, EDX, XRD and cyclic voltammetry. SEM

images and XPS data of Bi-PMo nanosheets before and after controlled potential electrolysis. Comparison of double layer capacitance and faradaic efficiencies for H_2 at different applied potentials obtained for Bi-PMo nanosheets and Bi nanodendrites. Controlled potential *i-t* curves and formate partial current densities at different applied potentials obtained for Bi-PMo nanosheets.

Conflict of Interest

The authors declare no conflict of interest.

Keywords

Electrochemical CO_2 reduction, formate, polyoxometalate, porous catalyst, ultrathin bismuth nanosheets

References:

[1] a) D. Voiry, H. S. Shin, K. P. Loh, M. Chhowalla, *Nat. Rev. Chem.* **2018**, *2*, 0105; b) F. Li, D. R. MacFarlane, J. Zhang, *Nanoscale* **2018**, *10*, 6235-6260; c) W. Bi, C. Wu, Y. Xie, *ACS Energy Lett.* **2018**, *3*, 624-633.

[2] H. Mistry, A. S. Varela, S. Kühl, P. Strasser, B. R. Cuenya, *Nat. Rev. Mater.* **2016**, *1*, 16009.

[3] S. Gao, Y. Lin, X. Jiao, Y. Sun, Q. Luo, W. Zhang, D. Li, J. Yang, Y. Xie, *Nature* **2016**, *529*, 68.

[4] L. Dai, Q. Qin, P. Wang, X. Zhao, C. Hu, P. Liu, R. Qin, M. Chen, D. Ou, C. Xu, S. Mo, B. Wu, G. Fu, P. Zhang, N. Zheng, *Sci. Adv.* **2017**, *3*.

[5] a) H. Zhong, Y. Qiu, T. Zhang, X. Li, H. Zhang, X. Chen, *J. Mater. Chem. A* **2016**, *4*, 13746-13753; b) S. Kim, W. J. Dong, S. Gim, W. Sohn, J. Y. Park, C. J. Yoo, H. W. Jang, J.-L. Lee, *Nano Energy* **2017**, *39*, 44-52; c) C. W. Lee, J. S. Hong, K. D. Yang, K. Jin, J. H. Lee, H.-Y. Ahn, H. Seo, N.-E. Sung, K. T. Nam, *ACS Catal.* **2017**; d) J. H. Koh, D. H. Won, T. Eom, N.-K. Kim, K. D. Jung, H. Kim, Y. J. Hwang, B. K. Min, *ACS Catal.* **2017**, 5071-5077; e) F. P. García de Arquer, O. S. Bushuyev, P. Luna, C.-T. Dinh, A. Seifitokaldani, M. I. Saidaminov, C.-S. Tan, L. N. Quan, A. Proppe, M. G. Kibria, S. O. Kelley, D. Sinton, E. H. Sargent, *Adv. Mater.* **2018**, *30*, 1802858; f) N. Han, Y. Wang, H. Yang, J. Deng, J. Wu, Y. Li, Y. Li, *Nat. Commun.* **2018**, *9*, 1320; g) S. Liu, Z. Luo, J. Guo, A. Pan, Z. Cai, S. Liang, *Electrochem. Commun.* **2017**, *81*, 10-13; h) P. Su, W. Xu, Y. Qiu, T. Zhang, X. Li, H. Zhang, *ChemSusChem* **2018**, *11*, 848-853; i) H. Zhang, Y. Ma, F. Quan, J. Huang, F. Jia, L. Zhang, *Electrochem. Commun.* **2014**, *46*, 63-66; j) W. Lv, J. Bei, R. Zhang, W. Wang, F. Kong, L. Wang, W. Wang, *ACS Omega* **2017**, *2*, 2561-2567; k) Y. Zhang, X. Zhang, Y. Ling, F. Li, A. M. Bond, J. Zhang, *Angew. Chem. Int. Ed.* **2018**, *57*, 13283-13287.

[6] a) J. L. DiMeglio, J. Rosenthal, *J. Am. Chem. Soc.* **2013**, *135*, 8798-8801; b) Z. Zhang, M. Chi, G. M. Veith, P. Zhang, D. A. Lutterman, J. Rosenthal, S. H. Overbury, S. Dai, H. Zhu, *ACS Catal.* **2016**, *6*, 6255-6264; c) J. Medina-Ramos, S. S. Lee, T. T. Fister, A. A. Hubaud, R. L. Sacci, D. R. Mullins, J. L. DiMeglio, R. C. Pupillo, S. M. Velardo, D. A. Lutterman, J. Rosenthal, P. Fenter, *ACS Catal.* **2017**, *7*, 7285-7295.

[7] P. Hofmann, *Prog. Surf. Sci.* **2006**, *81*, 191-245.

[8] D. L. Partin, J. Heremans, D. T. Morelli, C. M. Thrush, C. H. Olk, T. A. Perry, *Phys. Rev. B* **1988**, *38*, 3818-3824.

[9] R. Gusmão, Z. Sofer, D. Bouša, M. Pumera, *Angew. Chem. Int. Ed.* **2017**, *56*, 14417-14422.

[10] H. Hao, R. Xiaohui, L. Zhongjun, W. Huide, H. Zongyu, Q. Hui, T. Pinghua, Z. Jinlai, L. Weiyuan, G. Yanqi, L. Jie, L. Jianqing, Q. Xiang, Z. Han, *Nanotechnology* **2018**, *29*, 235201.

[11] L. Escobar-Alarcón, E. Velarde Granados, D. A. Solís-Casados, O. Olea-Mejía, M. Espinosa-Pesqueira, E. Haro-Poniatowski, *Appl. Phys. A* **2016**, *122*, 433.

[12] S. Liu, Z. Luo, J. Guo, A. Pan, Z. Cai, S. Liang, *Electrochem. Commun.* **2017**, *81*, 10-13.

[13] N. Reim, A. Littig, D. Behn, A. Mews, *J. Am. Chem. Soc.* **2013**, *135*, 18520-18527.

[14] C. H. Chen, K. D. Kepler, A. A. Gewirth, B. M. Ocko, J. Wang, *J. Phys. Chem.* **1993**, *97*, 7290-7294.

[15] A. Ananthi, S. S. Kumar, K. L. Phani, *Electrochim. Acta* **2015**, *151*, 584-590.

[16] M. Yang, *J. Mater. Chem.* **2011**, *21*, 3119-3124.

[17] M. Biçer, H. Köse, İ. Şişman, *J. Phys. Chem. C* **2010**, *114*, 8256-8263.

[18] a) Y. Wang, I. A. Weinstock, *Chem. Soc. Rev.* **2012**, *41*, 7479-7496; b) J. Zhang, B. P. Ting, Y. T. Koh, J. Y. Ying, *Chem. Mater.* **2011**, *23*, 4688-4693; c) C. L. Leng, Z. Jie, Y. Jinhua, A. Makhlouf, Y. J. Y., *Adv. Syn. Catal.* **2011**, *353*, 2988-2998; d) G. Zhang, B. Keita, A. Dolbecq, P. Mialane, F. Sécheresse, F. Miserque, L. Nadjo, *Chem. Mater.* **2007**, *19*, 5821-5823.

[19] S.-X. Guo, F. Li, L. Chen, D. R. MacFarlane, J. Zhang, *ACS Appl. Mater. Interfaces* **2018**, *10*, 12690-12697.

[20] F. Li, L. Chen, G. P. Knowles, D. R. MacFarlane, J. Zhang, *Angew. Chem. Int. Ed.* **2017**, *56*, 505-509.

[21] S. Himeno, M. Takamoto, T. Ueda, *J. Electroanal. Chem.* **2000**, *485*, 49-54.

[22] a) S.-X. Guo, S. W. Feldberg, A. M. Bond, D. L. Callahan, P. J. S. Richardt, A. G. Wedd, *J. Phys. Chem. B* **2005**, *109*, 20641-20651; b) Y. Liu, S.-X. Guo, A. M. Bond, J. Zhang, Y. V. Geletii, C. L. Hill, *Inorg. Chem.* **2013**, *52*, 11986-11996.
[23] M.-Y. Liu, Y. Huang, Q.-Y. Chen, Z.-Y. Li, C. Cao, Y. He, *RSC Advances* **2017**, *7*, 39546-39555.
[24] a) A. K. Cuentas-Gallegos, C. Frausto, L. A. Ortiz-Frade, G. Orozco, *Vib. Spectrosc.* **2011**, *57*, 49-54; b) C. Rocchiccioli-Deltcheff, M. Fournier, R. Franck, R. Thouvenot, *Inorg. Chem.* **1983**, *22*, 207-216.
[25] a) M. Dieterle, G. Mestl, *PCCP* **2002**, *4*, 822-826; b) L. Seguin, M. Figlarz, R. Cavagnat, J. C. Lassègues, *Spectrochim. Acta, Part A* **1995**, *51*, 1323-1344.
[26] a) K. Latha, L. Jin-Han, M. Yuan-Ron, *J. Phys.: Condens. Matter* **2007**, *19*, 406204; b) V. N. Denisov, A. N. Ivlev, A. S. Lipin, B. N. Mavrin, V. G. Orlov, *J. Phys.: Condens. Matter* **1997**, *9*, 4967.
[27] a) Z. Yang, Z. Tengfei, Z. Xudong, P. W. Kong, G. Hong, L. Sean, Z. Zhen, L. Huakun, G. Zaiping, *Adv. Mater.* **2017**, *29*, 1700396; b) W. Wei, J. Gao, Z. Jiang, X. Lü, J. Xie, *Ceram. Int.* **2015**, *41*, 11471-11481.
[28] J. Baltrusaitis, B. Mendoza-Sanchez, V. Fernandez, R. Veenstra, N. Dukstiene, A. Roberts, N. Fairley, *Appl. Surf. Sci.* **2015**, *326*, 151-161.
[29] NIST X-ray Photoelectron Spectroscopy Database, Version 4.1 (National Institute of Standards and Technology, Gaithersburg, 2012); http://srdata.nist.gov/xps/.
[30] R. Nyholm, A. Berndtsson, N. Martensson, *J. Phys. C: Solid State Phys.* **1980**, *13*, L1091.
[31] a) V. S. Dharmadhikari, S. R. Sainkar, S. Badrinarayan, A. Goswami, *J. Electron Spectrosc. Relat. Phenom.* **1982**, *25*, 181-189; b) T. P. Debies, J. W. Rabalais, *Chem. Phys.* **1977**, *20*, 277-283; cK. Uchida, A. Ayame, *Surf. Sci.* **1996**, *357-358*, 170-175.
[32] D. A. G. van Oeffelen, J. H. C. van Hooff, G. C. A. Schuit, *J. Catal.* **1985**, *95*, 84-100.
[33] a) M. J. Deery, O. W. Howarth, K. R. Jennings, *J. Chem. Soc.*, *Dalton Trans.* **1997**, 4783-4788; b) C. E. Easterly, D. M. Hercules, M. Houalla, *Appl. Spectrosc.* **2001**, *55*, 1671-1675.
[34] F. Li, L. Chen, M. Xue, T. Williams, Y. Zhang, D. R. MacFarlane, J. Zhang, *Nano Energy* **2017**, *31*, 270-277.
[35] S. Fletcher, *J. Solid State Electrochem.* **2009**, *13*, 537-549.
[36] D. Gao, H. Zhou, J. Wang, S. Miao, F. Yang, G. Wang, J. Wang, X. Bao, *J. Am. Chem. Soc.* **2015**, *137*, 4288-4291.
[37] X. Xi, S. Dong, *Electrochim. Acta* **1995**, *40*, 2785-2790.

Table of Contents

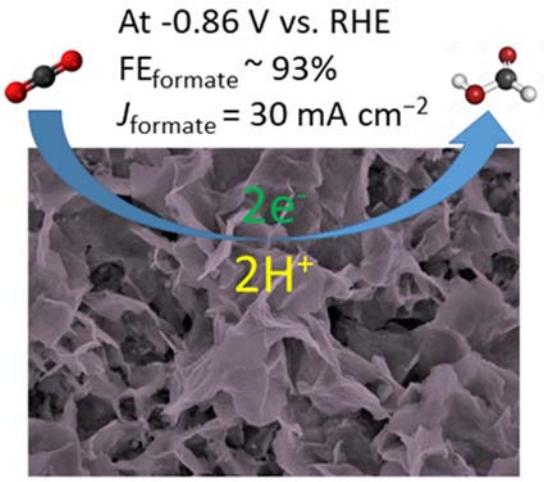

Hydrogen bubble templated electrodeposition of bismuth in the presence of phosphomolybdic acid leads to the formation of a three dimensional electrode consisting of interconnected bismuth nanosheets of 4 nm thick. This electrode exhibits excellent catalytic activity and selectivity for CO_2 reduction to formate in an aqueous bicarbonate medium.